



Highly efficient degradation of sulfur-containing volatile organic compounds by amorphous MnO₂ at room temperature: Implications for controlling odor pollutants

Jiangping Liu ^{a,c,1}, Hong Su ^{a,1}, Yanan Hu ^{a,b,c,*}, Chenhao Gong ^{a,c}, Jichang Lu ^{a,c}, Dedong He ^{b,c}, Wenjie Zhu ^{a,c}, Dingkai Chen ^{b,c}, Xiaohua Cao ^{b,c}, Jun Li ^d, Sasho Gligorovski ^e, Yongming Luo ^{a,b,c,*}

^a Faculty of Environmental Science and Engineering, Kunming University of Science and Technology, Kunming 650500, China

^b Faculty of Chemical Engineering, Kunming University of Science and Technology, Kunming 650500, China

^c The Innovation Team for Volatile Organic Compounds Pollutants Control and Resource Utilization of Yunnan Province, The Higher Educational Key Laboratory for Odorous Volatile Organic Compounds Pollutants Control of Yunnan Province, Kunming 650500, China

^d Henan Institute of Advanced Technology, Zhengzhou University, Zhengzhou 450052, China

^e State Key Laboratory of Organic Geochemistry, Guangzhou Institute of Geochemistry, Chinese Academy of Sciences, Guangzhou 510 640, China



ARTICLE INFO

Keywords:

S-VOCs
Amorphous MnO₂
Room Temperature
Reaction Mechanism
Environmental Implication

ABSTRACT

Sulfur-Containing Volatile Organic Compounds (S-VOCs) are notorious for global air pollution due to their odorous characteristics and exhibiting adverse health effects. Nevertheless, the catalytic degradation of S-VOCs at low temperatures is still a tremendous challenge for air purification. In this study, methyl mercaptan (CH₃SH), a typical S-VOCs contaminant, could be completely removed by amorphous MnO₂ with high efficiency (100 %) for 40 h at room temperature, and demonstrating significantly enhanced stability (over 100 h) in the presence of 20 %RH (Relative humidity), which is far superior to the performance of previous reported catalysts. The amorphous MnO₂ with surface-rich oxygen vacancies can trigger the formation of more reactive oxygen species (ROS) and stronger O₂ adsorption capability comparing with the crystalline MnO₂, the corresponding results are characterized by XPS and EPR. Moreover, *In Situ*-DRIFTS coupled with DFT calculations revealed that the CH₃SH could be transformed into CO₃²⁻/SO₄²⁻ by ROS. Unexpectedly, the amorphous MnO₂ also displayed excellent activity and stability towards to other typical S-VOCs, which is beneficial for the actual industrial application. The findings can provide novel insights into the design of highly efficient and stable catalysts to eliminate odor gaseous pollutants over a broad operating concentration window at room temperature.

1. Introduction

Growing concern about air quality stresses the importance of developing remediation technologies for eliminating malodorous pollution. As representative odorous air pollutants, sulfur-containing volatile organic compounds (S-VOCs) were believed to be one of the important potential precursor pollutants contributing to the formation of photochemical smog and urban haze, thereby exerts a significant influence on the air quality and human health [1–3]. Methyl mercaptan (CH₃SH) is a typical S-VOCs in the atmosphere, which is mainly emitted from sewage treatment, sanitary landfills and industrial waste sources

[4,5]. In addition, the presence of few ppb-level CH₃SH will lead to an unpleasant smell and even give rise to adverse health effects on the human body with the expose to high concentration (ppm-level). Currently, catalytic degradation process is considered as the most promising approach for S-VOCs removal because of its high purification efficiency, low energy consumption and less secondary products [6,7]. Over the past few years, a large number of catalysts have been widely used for the catalytic decomposition of CH₃SH such as zeolites [8–10] and metal oxides (CeO₂, Cr₂O₃ and so on) [11–13]. However, the widespread application of these catalysts is held back by their high operation temperature (>450 °C), low efficiency and secondary

* Corresponding authors at: Faculty of Environmental Science and Engineering, Kunming University of Science and Technology, Kunming 650500, China.

E-mail addresses: 18213071158@163.com (Y. Hu), environcatalysis@kust.edu.cn (Y. Luo).

¹ These authors contributed equally to this work

pollution formation, which are unsuitable for industrial activities with emission concentrations ranging from few to hundreds of ppm. Thus, developing the facile and efficient catalysts for S-VOCs removal at various concentrations under room temperature, to meet the requirements for the protection of human health and mitigation of air pollution is urgently needed.

According to the previous studies, transition metal oxides-based catalysts have been developed as efficient catalysts for the catalytic decomposition of VOCs due to their high activity, low cost and availability [14]. Among the transition metal oxides, MnO₂-based catalysts have attracted increasing attention due to their advantageous of catalytic properties, plentiful valence states and low operation cost [15]. Recently, the MnO₂-based and its modified catalysts have developed as one of the most promising methods for CH₃SH elimination [16–18]. For instance, Ag deposited three-dimensional MnO₂ porous hollow microspheres showed 100 % conversion of 70 ppm CH₃SH during period of 10 min [16]. Three facet-engineered α -MnO₂ was prepared and successfully applied for the catalytic ozonation towards CH₃SH, the as-synthesized 310-MnO₂ exhibited completely degrade for 70 ppm of CH₃SH within 20 min [17]. A recent study demonstrated enhanced CH₃SH elimination of 96.9 % conversion on optimum Ag/R-MnO₂ compared to the pristine R-MnO₂ under GHSV of 75,000 mL h⁻¹ g⁻¹ [19]. Although extensive laboratory studies have reported that the low concentration of CH₃SH can be eliminated by MnO₂-based catalysts at room temperature, the catalytic ozonation process still suffers from low operation stability and additional introduction of ozone (O₃). In particular, a large amount of O₃ can also be released into the atmosphere in the ozonation process, which could further exacerbate the global O₃ pollution problems today. More importantly, the removal of CH₃SH by MnO₂-based catalysts at room temperature is still hampered by poor operating stability in the presence of O₂ or O₃, and its removal and conversion mechanism remain unclear. Motivated by these issues, particular attention should be paid to seeking for an approach to provide widespread and efficient reaction conditions (in the absence of O₂ or O₃) for the catalytic degradation of CH₃SH at room temperature and then transformed it into CO₃²⁻/SO₄²⁻ or converted to other relatively less toxic product efficiently.

Previous studies have confirmed that surface defects, especially oxygen vacancies, are the primary active sites for inducing catalytic decomposition of organic molecules [20,21]. Birnessite-MnO₂ (i.e., δ -MnO₂) is a unique layer structure that is composed of [MnO₆] octahedra, which has poorly crystalline (disordered), layered structures and are widely distributed minerals [22]. Amorphous MnO₂ catalysts have aroused particular interest for heterogeneous reaction due to their distorted lattice structure and intrinsic properties of oxygen migration, however, they have not attracted extensively studied when compared to their crystalline structure [23]. The particular structure makes amorphous MnO₂ exhibit many special features, such as the coexistence of different valence states, abundant oxygen vacancies and manifest great flexibility to regulate their active sites [23,24], which showed great potential for VOCs removal. Prior research works have been developed for degradation of VOCs at low temperatures by various novel strategies [25–27]. To date, the removal and stability of CH₃SH from amorphous MnO₂ at room temperature and its removal mechanism has not been evaluated yet. To our knowledge, a novel investigation on the amorphous MnO₂ applied for the catalytic decomposition of 100 ppm-level CH₃SH at ambient temperature was explored. The as-synthesized amorphous MnO₂ achieved excellent activity and superior stability for CH₃SH catalytic conversion over 40 h long-term test, which is attributed to the formation of abundant active oxygen species on the amorphous MnO₂ surface with plenty of structural defects compared to commercial MnO₂. The results were confirmed by the characterization of high-resolution transmission electron microscopy (HRTEM), X-ray photoelectron spectroscopy (XPS) and Electron paramagnetic resonance (EPR). The reaction mechanisms were also explored by *in situ* diffuse reflectance infrared Fourier transform spectroscopy (DRIFTS) and Density Functional Theory (DFT) calculation. Finally, the deactivated

catalysts can be regenerated and reused via the simple washing method to remove the accumulated species. This study can provide a novel insight for the design of optimized catalysts and its further application to eliminate odorous gases such as one-component and multi-component mercaptans at room temperature in the atmosphere.

2. Materials and methods

2.1. Catalyst preparation

B-MnO₂ catalysts were synthesized through the hydrothermal method as previously reported [28]. In detail, 3.16 g KMnO₄ and 1.42 g (NH₄)₂C₂O₄ were dissolved in 70 mL deionized water with magnetic stirring for 2 h to form a homogeneous suspension. Then the liquids were instantly transferred into 100 mL Teflon-lined stainless-steel autoclaves and put into an oven to maintain the temperature at 90 °C for 24 h. After cooling down naturally to room temperature, the resulting precipitates were collected by centrifugation and washed with deionized water three or four times. Finally, the products were dried at 105 °C for 12 h. The obtained powders were denoted as B-MnO₂, and the commercial manganese oxide is named C-MnO₂ (A-MnO₂ and α -MnO₂ were prepared as the reference according to previous work) [24]. Besides, the hydrothermal method was employed to fabricate B-MnO₂ as shown in Fig. S1.

2.2. Catalyst characterization

X-ray diffraction (XRD) patterns of as-prepared samples were recorded on an X-ray diffractometer (D/Max-2200, Rigaku, Japan) using Cu K α irradiation ($k = 0.154054$ nm), operating at 30 mA and 40 kV. The scanning electron microscopy (SEM, VEGA3SBH, Czech Republic) and high-resolution transmission electron microscopy (HRTEM, Talos F200X, Thermo Scientific, USA) were used to detect morphologies. X-ray photoelectron spectroscopy (XPS) of samples were recorded on an ESCALAB 250XI spectrometer (XPS, Esca lab 250Xi, Thermos Fisher Scientific, USA) using an Al K α X-ray source. Electron paramagnetic resonance (EPR) was performed on a Bruker EPR 300E spectrometer, and 5,5-dimethyl-l-pyrroline N-oxide (DMPO) was used as the trapping agent to investigate the formation of ROS at 25 °C. The final catalytic products of CH₃SH were analyzed by an ion chromatography (IC, AQUION, Thermos Fisher Scientific, USA).

Hydrogen temperature-programmed reduction (H₂-TPR) and oxygen temperature-programmed desorption (O₂-TPD) experiments were performed on a FULI II 7970 gas chromatography with a thermal conductivity detector (TCD). In H₂-TPR experiments, 50 mg of sample was placed in a quartz tube and pretreated in a gas flow of 10 % He (30 mL/min) at 100 °C for 30 min to remove impurities. After the pretreatment process, the sample was reduced by 10 % H₂/Ar (30 mL/min) from 100 to 800 °C with a heating rate of 10 °C/min. For O₂-TPD analysis, 50 mg of sample was loaded on the quartz tube, heated to 105 °C and pretreated with He (30 mL/min) for 30 min to remove surface adsorbed water, followed by cooling to 30 °C. Subsequently, the sample adsorbed 10 % O₂/He (30 mL/min) at room temperature for 60 min, and then the He flow (30 mL/min) was used to purge the sample for 30 min to remove physically adsorbed O₂ and stabilize the baseline, the temperature was controlled from 30 to 850 °C at a rate of 10 °C/min.

In situ diffuse reflectance infrared Fourier transform spectroscopy (DRIFTS) was recorded on a Nicolet iS50 FT-IR (Thermo Fisher, America). An *in-situ* cell was applied to detect the change of surface functional groups of catalysts during the CH₃SH catalytic reaction. For the room-temperature adsorption and catalysis, the sample (20 mg) was pretreated in pure N₂ (25 mL/min) at 30 °C for 30 min and afterwards the background spectrum was recorded. Then, the CH₃SH (5000 ppm, N₂ as the balance gas) continuously flowed through the *in-situ* cell. Finally, the signal was collected.

2.3. Catalyst activity evaluation

The catalytic performance for the CH₃SH decomposition was investigated in a fixed-bed quartz tube reactor (i.d.=6 mm). 100 mg samples with the size of 40–60 meshes were loaded into the reactor. Under identical conditions, the reaction was maintained at each designed reaction temperature for approximately 1 h. The inlet CH₃SH concentration was set at 100 ppm, and the total flow rate was 120 mL/min with the corresponding gas hourly space velocity (GHSV) of 72 L g⁻¹ h⁻¹. The concentrations of CH₃SH were measured using GC-9790 (FULI, China) with a flame ionization detector (FID) and flame photometric detector (FPD), the CH₃SH conversion ratio was calculated as follows:

$$\text{CH}_3\text{SH conversion} = \frac{C_{in} - C_{out}}{C_{in}} \times 100\%$$

C_{in} represents the inlet concentration of CH₃SH and C_{out} is the outlet concentration of CH₃SH.

2.4. DFT calculations method

Vienna ab-initio simulation package (VASP) was employed [29,30] to perform all the spin-polarized density functional theory (DFT) calculations within the generalized gradient approximation (GGA) using the Perdew-Burke-Ernzerhof (PBE) [31] formulation. Projected augmented wave (PAW) potentials was used [32,33] to describe the ionic cores and take valence electrons into account using a plane wave basis set with a kinetic energy cutoff of 500 eV.

The equilibrium lattice constants of [C-MnO₂] unit cell was optimized, when using a 6 × 6 × 9 Monkhorst-Pack k-point grid for Brillouin zone sampling to be a= b= 4.45126, c= 2.88126 Å. These lattice constants were used to build the MnO₂ (101) surface slab with 4 at. layers, which contains 24 Mn atoms, and 48 O atoms. In addition, the equilibrium lattice constants of [B-MnO₂] unit cell was optimized, when using a 5 × 9 × 4 Monkhorst-Pack k-point grid for Brillouin zone sampling to be a= 5.91725, b= 2.99181, c= 7.59515 Å. These lattice constants were used to build the MnO₂ (001) surface slab with 6 at. layers, which contains 32 Mn atoms, and 96 O atoms. During structural optimizations of the models, a 3 × 3 × 1 gamma-point centered k-point grid for Brillouin zone was used. The crystal structure of C-MnO₂ and B-MnO₂ are shown in Fig. S2. Besides, the adsorption energy (E_{ads}) of an adsorbate A was defined as :

$$E_{ads} = E_{A/surf} - E_{surf} - E_A$$

where E_{A/surf}, E_{surf} and E_A are the energy of A adsorbed on the surface slab, the energy of surface slab, and the energy of adsorbates, respectively. However, it is important to note that, the crystallinity and amorphous MnO₂ catalyst are both of [MnO₆]⁴⁻, in addition, the broader and weaker peaks of B-MnO₂ located ~12.1°, ~25.3°, ~37.0° and ~65.8° can be attributed to the δ-MnO₂, and the main facet of δ-MnO₂ is MnO₂ (001). Therefore, we created a model of B-MnO₂ catalyst which can be compared with that of δ-MnO₂, these lattice constants were used to build the MnO₂ (001).

3. Results and discussion

3.1. Catalyst activity

The catalytic performance of C-MnO₂ and B-MnO₂ for low concentration CH₃SH (100 ppm) was carried out as a function of reaction temperature under the GHSV of 72 L g⁻¹ h⁻¹. As depicted in Fig. 1a, only 45 % of CH₃SH was removed in the gas-solid reaction process by the C-MnO₂ at room temperature, and then the conversion rate reached 100 % with the reaction temperature up to 400 °C. However, it is notable to point out that the 100 % of CH₃SH removal is obtained for the B-MnO₂ at room temperature, and the conversion efficiency remained a relatively

stable trend in the range of 30–400 °C. These results can be compared with the removal rate of 75 ppm CH₃SH (96.9 %) on the optimum Ag/R-MnO₂ (rambutan-like MnO₂) but in the process of catalytic ozonation [19]. In the case of Ag/R-MnO₂, the unique hierarchical composition of Ag/R-MnO₂ with strong metal-metal oxide interaction facilitates the dynamic electron replenishment, which presents a new strategy for boosting ozone activation and eliminating S-VOCs. Xia et al. also suggested that Ag deposited three-dimensional MnO₂ porous hollow microspheres can completely catalytic conversion 70 ppm CH₃SH within 600 s, indicate that ·OH and ¹O₂ are the dominant reactive species to CH₃SH ozonation removal, and this work also suggest that the Ag may work as active sites for the process [16]. Meanwhile, the CH₃SH removal efficiency on the pristine R-MnO₂ is around 80 % during the catalytic ozonation process pointing to higher catalytic activity of B-MnO₂ in this study. Additionally, the stability test of CH₃SH conversion was also explored over four catalysts prepared by different methods (Fig. 1b), the B-MnO₂ and A-MnO₂ could remained 100 % conversion of CH₃SH during the whole 30 h test, which exhibited the highest catalytic stability compared to the C-MnO₂ and α-MnO₂. These results showed amorphous manganese oxide own better adaptability towards CH₃SH than those crystallinity samples. In addition, the deactivated catalysts can be easily regenerated and reused by the simple washing method. As shown in Fig. 1c, the CH₃SH conversion by regenerated on B-MnO₂ still could be maintained at 100 % for 25 h and 90 % for 50 h. Considering that the catalytic stability of the catalyst in the presence of water vapor is very critical for practical application, the long-term stability of B-MnO₂ was carried out and compared with that in pure gaseous system in the presence of 20 %, 50 % and 80 %RH. As shown in Fig. 1d, the decomposition efficiency of B-MnO₂ has a negative effect on the catalytic performance at 80 %RH humidity, this is because excessive water molecules might cover the active sites of B-MnO₂ surface. Notably, the catalytic performance of CH₃SH was significantly enhanced when the humidity decreased to 20 %RH and 50 %RH, and achieved 100 % conversion for more than 100 h at 20 %RH, indicated that the water may act as reactant molecules and beneficial to oxygen activation [34]. Moreover, the products distribution of the outlet gas were also provided in the Fig. 1e, only gas phase CH₃SSCH₃ and very little CH₄ can be detected on both MnO₂ catalysts at the current condition. These experiments demonstrate that B-MnO₂ can completely remove CH₃SH at low temperatures and suggested that a slight decrease of catalytic activity even under extremely high humidity (80 %RH). Moreover, the catalytic performance of B-MnO₂ was superior to the vast majority of Mn-based catalysts that reported recently, as summarized in Fig. S3, Text S2 and Table S2. The structural stability of B-MnO₂ during the reaction is also investigated, the XRD results of used catalyst showed that the amorphous structure of B-MnO₂ is stable and even with the increase of temperature (Fig. S4a and S4b). To the best of our knowledge, there are no other studies related to the catalytic elimination of CH₃SH by B-MnO₂ at room temperatures to compare the results presented here. Therefore, we aimed at elucidating a new perspective for understanding the superior performance of catalytic decomposition for CH₃SH removal at ambient temperatures, which indicates that the B-MnO₂ developed in this work has very high practical value and is very conducive to eliminating odorous gases in the real environment.

3.2. Characterization of Structure and Morphology

The structure of the material plays a crucial role in process of CH₃SH degradation. Thus, the crystal structure of the samples was investigated by XRD. As shown in Fig. 2a, the diffraction peaks are located ~28.7°, ~37.2°, ~42.7° and ~56.4° in the XRD patterns of C-MnO₂, which were consistent with the characteristic peaks of the pyrolusite-type MnO₂ (β-MnO₂, JCPDS No. 24-0735) with narrow peaks and high intensity, indicating its high crystallinity [35]. The broader and weaker peaks of B-MnO₂ located ~12.1°, ~25.3°, ~37.0° and ~65.8° can be attributed to the birnessite-type MnO₂ (δ-MnO₂, JCPDS No. 80-1098),

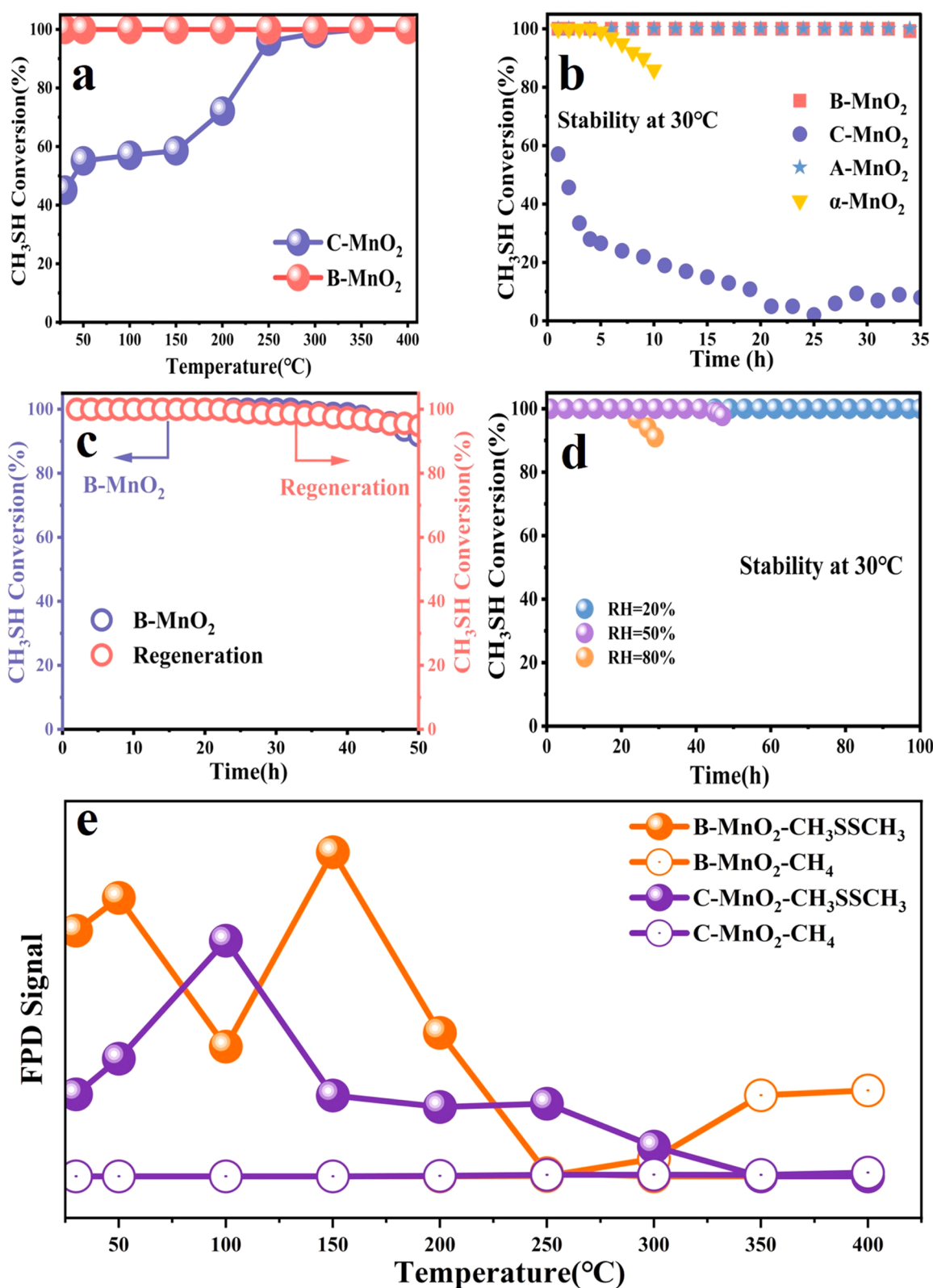


Fig. 1. Temperature profiles of CH_3SH conversion over the B- MnO_2 and C- MnO_2 catalysts (a); Catalyst stability test over B- MnO_2 , C- MnO_2 , A- MnO_2 and α - MnO_2 (b); Regenerated B- MnO_2 catalysts for long-term reaction at 30°C (c); CH_3SH decomposition test under high humidity conditions (d); (Reaction condition: 0.1 g of catalyst, $120 \text{ mL}\cdot\text{min}^{-1}$ of synthetic N_2 with 100 ppm of CH_3SH , RH=20 %, 50 % and 80 %); The products of distribution of CH_3SH decomposition reaction on B- MnO_2 and C- MnO_2 at 30°C (e).

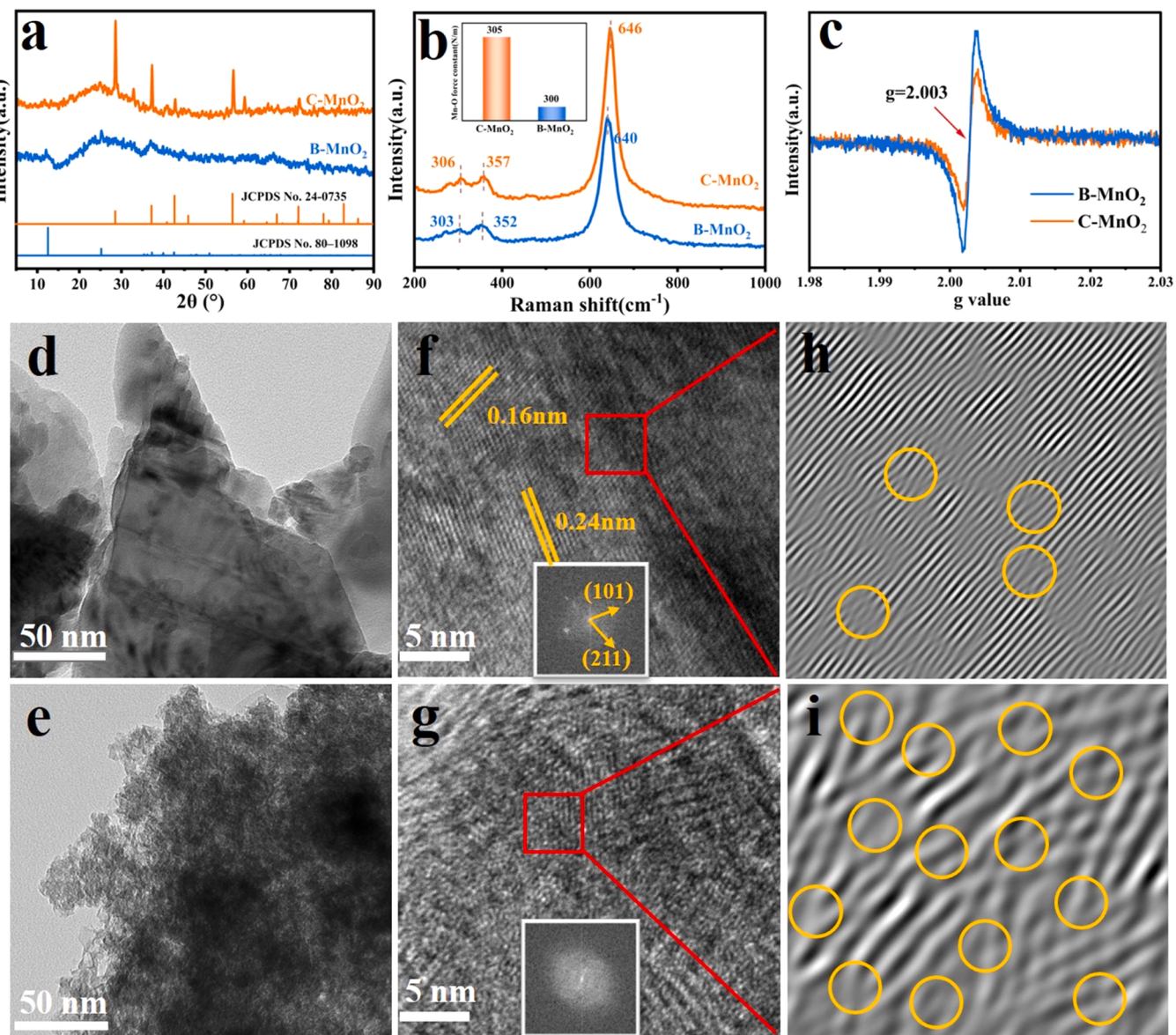


Fig. 2. XRD profiles of C-MnO₂ and B-MnO₂ (a); Raman spectra of C-MnO₂ and B-MnO₂ (b); EPR profiles of C-MnO₂ and B-MnO₂ (c); TEM (d, e) and HRTEM (f, g) images of C-MnO₂ and B-MnO₂, respectively; The inverse FFT patterns of C-MnO₂ (h) and B-MnO₂ (i), respectively.

demonstrating its poor crystallinity and amorphous nature [36]. Raman spectra further confirmed the low degree of crystallinity of the two samples in Fig. 2b. The different peaks around 640 cm⁻¹, 350 cm⁻¹ and 300 cm⁻¹ correspond to the second-order Raman scattering and stretching vibration, respectively, were detected in both samples. The weak intensity of peaks at 300 and 350 cm⁻¹ suggested the low crystallinity of the samples [37]. The weaker sharp vibrational peak near 640 cm⁻¹ also indicates low crystallinity of B-MnO₂ and more defects formation due to lattice distortion (Consistent with XRD (Fig. 2a)). Crystal distortion has been reported to alter the bond length between metal and oxygen are often accompanied by creating more oxygen vacancies, which was generally thought to affect the redox performance of the catalyst [38]. Therefore, according to Hooke's law [39], the following equation was used to calculate the Mn-O bond force constant (k), which represents the Mn-O bond strength.

$$\omega = \frac{1}{2\pi c} \sqrt{\frac{k}{\mu}}$$

where ω is the Raman shift (cm⁻¹), c is light velocity, and μ is the effective mass of the Mn-O bond. The calculated Mn-O force constant (k) was shown inset of Fig. 2b. The Mn-O bond force constant (k) of B-MnO₂ (300 N/m) was smaller than that of C-MnO₂ (305 N/m), implying a weaker Mn-O bond. This result reveals that a weaker Mn-O bond can increase surface lattice oxygen activity and redox properties, thus increasing the activity of CH₃SH.

The morphologies and defects of two catalysts were detected by TEM and HRTEM. The TEM image (Fig. 2d) presents a block structure as well as the HRTEM (Fig. 2f) that showed the arranged lattice fringes for C-MnO₂. The two sets of the lattice spacing of C-MnO₂ are 0.18 nm and 0.24 nm, corresponding to (101) and (211) planes, respectively. Therefore, the TEM and HRTEM results indicate excellent crystallinity of C-MnO₂, which is well agreement with XRD and Raman analysis. The TEM (Fig. 2e) and HRTEM (Fig. 2g) images present fluffy and porous structure for B-MnO₂. Interestingly, the HRTEM exhibited the amorphous structure of B-MnO₂. Meanwhile, no diffraction spots were detected in FFT pattern (inset of Fig. 2g) of B-MnO₂, indicating the existence of amorphous structure as well as more defects formation on the

surface [36,40]. Besides, the presence of defects is further demonstrated using the inverse FFT pattern (Fig. 2h, i). It can be seen that abundant layer mismatches were clearly observed in B-MnO₂ (Fig. 2i), leading to blurring diffraction spots and disks. Hence, the intrinsic defective structure of B-MnO₂ was confirmed. Such defects are probable to contribute to the formation of oxygen vacancies. The above observations are well-matched with the inferences from HRTEM images. At the same time, previous studies have shown that Birnessite-MnO₂ is a layered crystalline oxide consisting of octahedral MnO₆, which is often accompanied by the formation of Mn defects and oxygen vacancies during the crystallization process [34,41]. These defects formed on amorphous B-MnO₂ play important roles in the catalytic decomposition of organic compounds. The N₂ adsorption-desorption experiments were performed to explore the effect of textural properties on two samples. It can be seen in Fig. S5 that both two samples display type IV adsorption isotherms, which are characteristic of mesoporous materials. The specific surface area and pore volume of B-MnO₂ and C-MnO₂ are listed in the Table S1. These results showed that the B-MnO₂ owned larger specific surface area and pore volume than the C-MnO₂ catalyst, which could provide more active sites for determining the activity of CH₃SH degradation. Meanwhile, the crystallinity of the B-MnO₂ calcined by different temperatures are also investigated, the results showed that there is no obvious effect on the catalytic performance of CH₃SH removal, and the amorphous crystallinity of B-MnO₂ after reaction with CH₃SH remained stable without any change (Fig. S4a-c) and Text S3). The change of morphologies during the reaction was determined by SEM, TEM and HRTEM characterizations (Fig. S6). It can be concluded that the B-MnO₂ after reaction always retained poor crystallinity and amorphous structure, suggesting that the crystal plane structure reconstruction of the B-MnO₂ during the reaction did not occur. To better compare the catalytic activity between amorphous MnO₂ and high crystallinity (α -MnO₂), the CH₃SH decomposition activities over these catalysts were further evaluated. The results confirmed that amorphous manganese oxide own better catalytic performance towards CH₃SH than that of crystallinity samples, more details about this discussion could be seen in Fig. S4d, S4e and Text S3.

The surface chemical valance detected by XPS was used to prove the presence of defects on the catalyst surface. Generally, the catalytic performance of CH₃SH conversion is closely related to surface defects

[16,17]. The XPS spectra of Mn 3 s and Mn 2p_{3/2} orbit of the samples are shown in Fig. 3a, b and Fig. 3c, d, the average oxidation state (AOS) of the surface Mn atoms was calculated by AOS= 8.956–1.126ΔEs, where ΔEs represents the splitting width between the two Mn 3 s peaks [42]. As displayed in Fig. 3a and b, the splitting energies of C-MnO₂ and B-MnO₂ are 4.7 eV and 4.9 eV, respectively, corresponding to the AOS for Mn atoms on two samples, i.e., 3.66 and 3.44. The lower AOS of B-MnO₂ is mainly results from the more low-valent Mn in the sample. The Mn 2p_{3/2} spectra could be divided into two characteristic peaks with the binding energy at 640.3–641.0 eV, 641.6–641.9 eV and 642.9–643.0 eV, corresponding to Mn²⁺, Mn³⁺ and Mn⁴⁺, respectively (Fig. 3c, d) [43]. It is clear that the proportions of low valance Mn (Mn²⁺ and Mn³⁺) in B-MnO₂ (38 %) was higher than that in C-MnO₂ (28.5 %) as shown in Table S1. The more low-valent Mn (Mn²⁺ and Mn³⁺) presented on MnO₂ represents more Mn-O bonds of longer length and weaker binding energy on the surface of MnO₂ [44,45], making it easier to release oxygen atoms from the MnO₂ surface and induce more oxygen vacancies form on the catalyst surface, which is consistent with the Raman results (Fig. 2b). The oxygen vacancies concentration is slightly higher for B-MnO₂ as it has a stronger EPR signal than C-MnO₂ at g= 2.003 (Fig. 2c). The above-mentioned results further proved the more oxygen vacancies formed on the surface of B-MnO₂ and the catalytic activity of CH₃SH is related to oxygen vacancy.

3.3. Characterization of oxygen species

The type and content of oxygen species were determined by O 1 s spectra. As shown in Figs. 3e and 3f, the binding energy at 529.4–529.7 eV, 530.9–531.1 eV and 532.7–533.2 eV was assigned to the lattice oxygen (O_{latt}), low coordination number surface adsorbed oxygen species (O_{ads}), and H₂O/OH species (O_{H2O+OH}), respectively [46, 47]. Based on the results of TG (Fig. S7 and Text S4), the H₂O/OH species were also detected and should be considered as the surface adsorbed oxygen species. It was obvious to see that B-MnO₂ (38.5 %) contributes to the higher surface-adsorbed oxygen species than those of C-MnO₂ (34.6 %). The previous literature demonstrated that O_{ads} are usually adsorbed on the oxygen vacancies of mental oxide, and the content of O_{ads} is highly dependent on surface oxygen vacancy [48,49]. Similarly, the proportions of Mn²⁺+Mn³⁺/Mn⁴⁺ and O_{ads}/O_{latt}

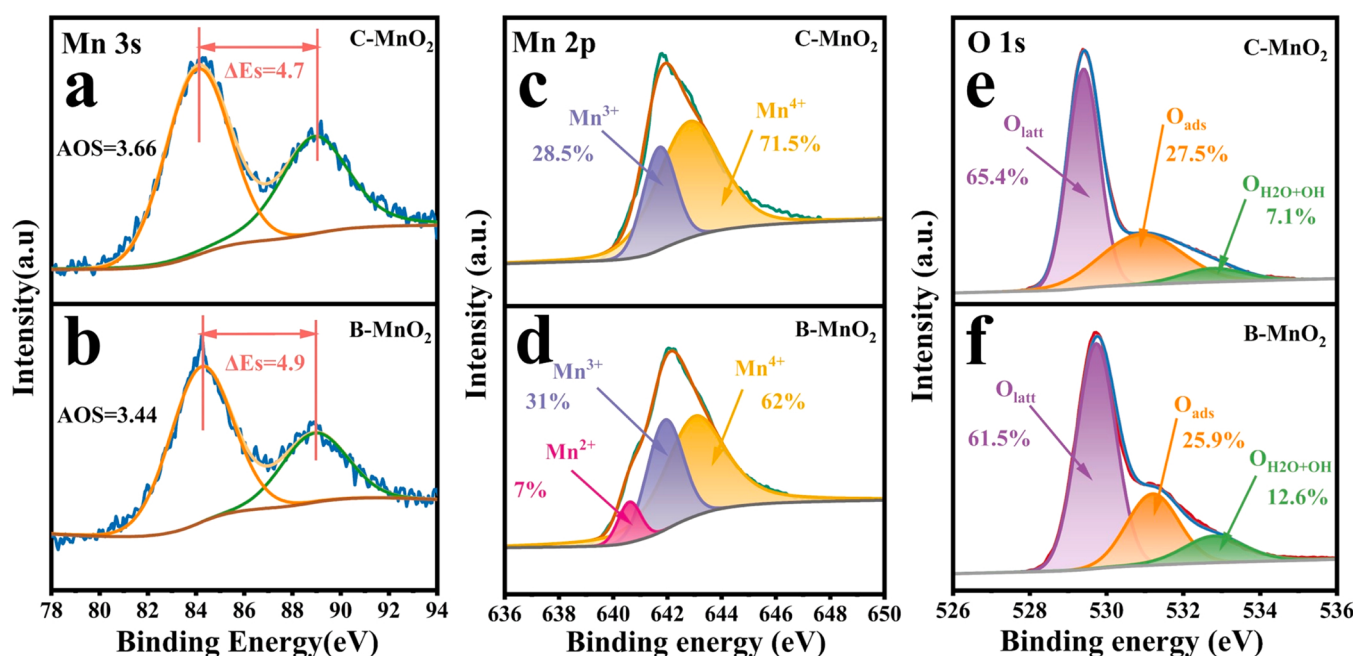


Fig. 3. XPS spectra of Mn 3 s (a, b), Mn 2p_{3/2} (c, d) and O 1 s (e, f) for C-MnO₂ and B-MnO₂, respectively.

corresponding to B-MnO₂ were 0.61 and 0.63, respectively, larger than that of C-MnO₂ (0.4 and 0.53), confirming that the lower AOS and more oxygen vacancies formation on B-MnO₂ than C-MnO₂. The oxygen vacancies on the surface of B-MnO₂ usually serve as adsorption active sites, and then induce the formation of ROS to participate in catalytic reactions of CH₃SH conversion. Meanwhile, the localized electrons of oxygen vacancies can change the balanced electronic structure of the catalyst, resulting in the formation of surface-active oxygen species [19, 44, 45], thereby leading to more ROS that could participate in the reaction of CH₃SH conversion at room temperature.

The surface reducibility of the catalysts was investigated by H₂-TPR experiments, which is a key factor correlated with their redox activity. As displayed in Fig. 4a, the C-MnO₂ catalyst showed two peaks located about 315 and 460 °C, which can be assigned to Mn⁴⁺→Mn³⁺ and Mn³⁺→Mn²⁺, respectively [50]. For the B-MnO₂ catalyst, the peaks around 270 and 300 °C corresponded to the reduction of Mn⁴⁺→Mn³⁺ and Mn³⁺→Mn²⁺, respectively [51]. Besides, the main peaks for B-MnO₂ appeared at 240 °C, which could be attributed to the reduction of surface adsorbed oxygen species [52], which indicates B-MnO₂ has more surface adsorbed oxygen species and stronger reducibility.

Furthermore, the oxygen mobility of the as-synthesized catalysts was explored by O₂-TPD experiments. As shown in Fig. 4b, the peaks of O₂-TPD can be divided into three regions: physically adsorbed oxygen/surface active oxygen (<500 °C), subsurface lattice oxygen (500–600 °C), and bulk lattice oxygen (>600 °C), respectively [53, 54]. It can be seen that no peak can be observed below 500 °C in C-MnO₂, while an obvious peak at ~200 °C around in B-MnO₂, implying B-MnO₂ owned more physically adsorbed oxygen/surface active oxygen species, which is consistent with the XPS O 1 s and H₂-TPR results. Besides, the oxygen desorption can be observed at lower temperatures reflected on O₂-TPD, which means oxygen species on the B-MnO₂ surface are more

prone to migration at low temperatures. Based on the above information, it can conclude that B-MnO₂ has much more oxygen vacancies and better oxygen mobility, thus a large amount of ROS can be generated at room temperature to drive the CH₃SH conversion.

The formation of ROS on the two samples were also detected by EPR, which was carried out with DMPO (5, 5-dimethyl-l-pyrroline N-oxide) as the trapping agent, and the results are shown in Fig. 4c and d. No signal can be detected in C-MnO₂, indicating the absence of ROS. On the other hand, the B-MnO₂ sample exhibits a significantly enhanced signal compared to C-MnO₂, revealing a large number of ROS formation around the surface. The typical characteristic peaks in Fig. 4(c, d) could be assigned to ·O₂ and O₂^{·-}, respectively [55, 56]. Previous studies have reported that surface adsorbed oxygen can be activated by oxygen vacancies on MnO₂ to form O₂^{·-} and ·O₂ [37]. Furthermore, the oxygen vacancies belonging to single or two electron-trapped centers can trigger the adsorbed oxygen species to form ·O₂ or O₂^{·-} respectively [57]. These results clearly show that B-MnO₂ can produce far more ROS than C-MnO₂ by activating surface oxygen species through oxygen vacancies, which is expected to display better catalytic performance.

3.4. Possible Reaction Mechanism

The surface oxygen species are directly involved in the decomposition of CH₃SH, according to the results of XRD, HRTEM and EPR above, the reactivity of surface oxygen species are important factors to reflect the activity of the catalyst, thus the transformation behaviors of the catalysts before and after the reaction were investigated to identify the reaction mechanism. As revealed in Fig. 5a, b and Fig. S8, the oxygen species of the two samples both demonstrated less lattice oxygen and more adsorbed oxygen with the proceed of reaction. Since the reaction is performed under the condition of oxygen-free atmosphere, it can be

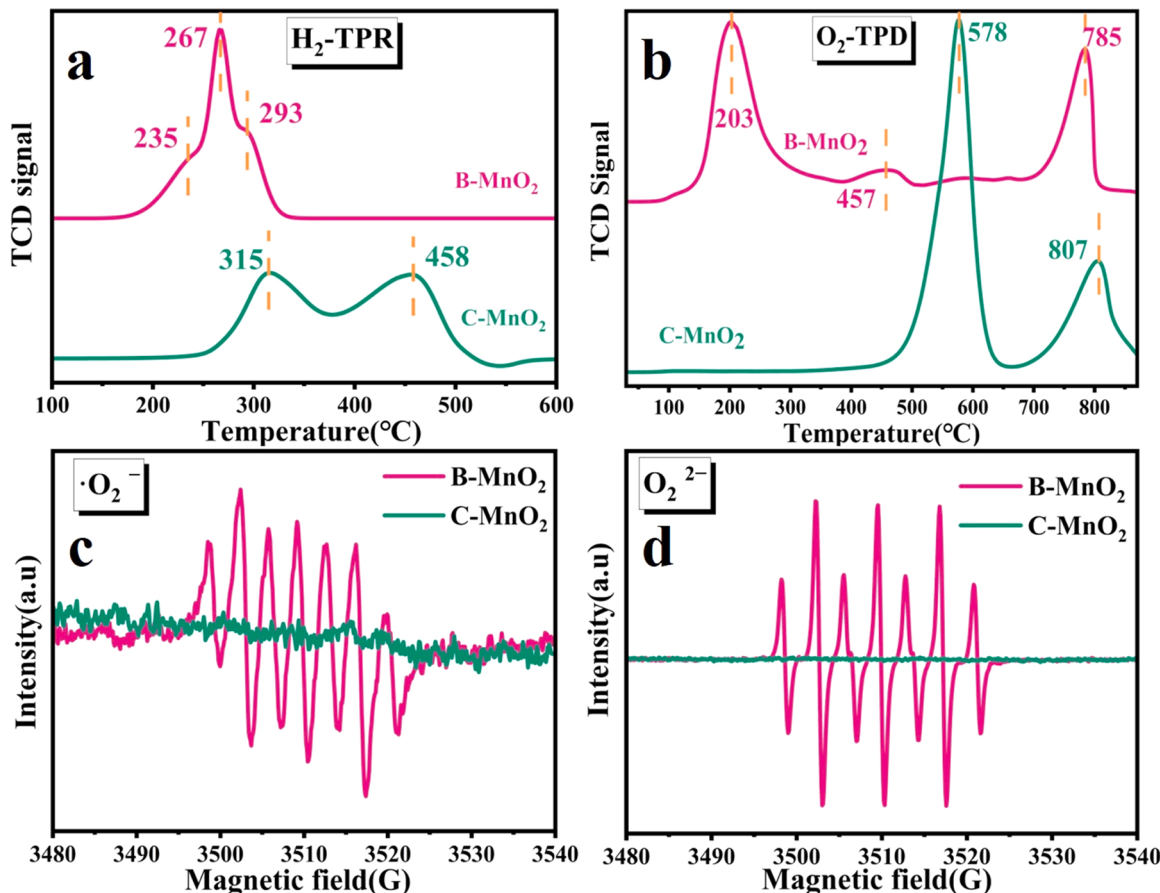


Fig. 4. Profile of H₂-TPR (a) and O₂-TPD (b), EPR signal of superoxide radical (·O₂) (c) and peroxy radical (O₂^{·-}) (d), respectively.

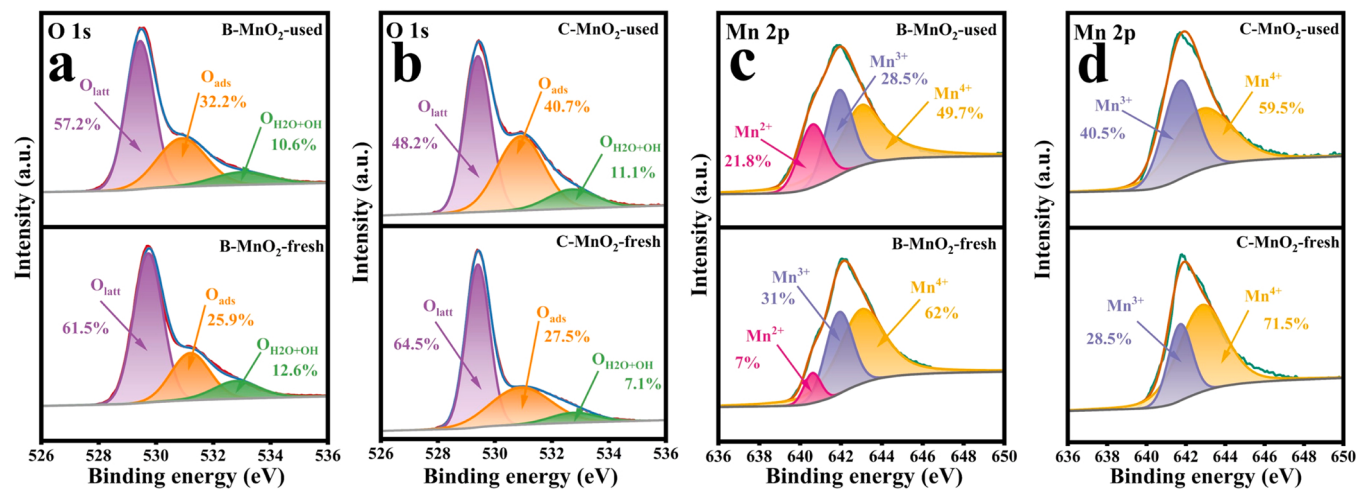


Fig. 5. XPS spectra of O 1 s for B-MnO₂-fresh, B-MnO₂-used (a) and C-MnO₂, C-MnO₂-used (b); Mn 2p for B-MnO₂-fresh, B-MnO₂-used (c) and C-MnO₂, C-MnO₂-used (d).

concluded that the increased surface adsorbed oxygen could be attributed to the migration of lattice oxygen based on XPS results [58]. Furthermore, the variations of Mn-O bond length between the two samples before and after adsorption were analyzed to further explore the transition between lattice oxygen and adsorbed oxygen. Fig. S9 illustrated the length of the Mn-O bond on B-MnO₂ (1.89 Å) is longer than that of C-MnO₂ (1.82 Å), indicating that the Mn-O bond on B-MnO₂ is more easily to break and then release lattice oxygen than C-MnO₂, well agreeing with the Raman result (Fig. 2b) [47]. Especially, the bond length of the Mn-O bond changed from 1.89 Å to 2.09 Å after the adsorption of CH₃SH on B-MnO₂, which is a huge variation (0.2 Å) compared with C-MnO₂ (0.03 Å), implying the electron cloud density between Mn-O became smaller and then leading to the Mn-O bond weaker. These results can be explained by the fact that the electrons are more likely to migrate easily to S during the adsorption for B-MnO₂ [59, 60]. As shown in Fig. S10 (S 2p) and Fig. S11 (C 1s), more sulfur and carbon-containing species are generated on B-MnO₂ surface (Text S4 and Text S5), suggesting that the lattice oxygen migrated from B-MnO₂ can better participate in the catalytic reaction compared to C-MnO₂ [61–63]. The results of O 1s (Fig. 5a and b) displayed more lattice oxygen can be migrated on C-MnO₂ than B-MnO₂ during the reaction, which is probably due to the fact that the release and consumption of lattice oxygen are simultaneous occur on B-MnO₂, while the lattice oxygen released from C-MnO₂ is not readily involved in the reaction [61]. The proportion of low valence Mn (Mn²⁺ and Mn³⁺) showed an obvious increment both on B-MnO₂ and C-MnO₂ (Fig. 5c and d), indicating that the lattice oxygen can be migrated and thus converted to the ROS, which agrees with the results of O 1s [64,65]. Based on the above analysis, lattice oxygen migration is more likely to occur on B-MnO₂ during the reaction, and the migrated lattice oxygen is more conducive to converted into ROS and then participating in the reaction. The turnover frequency (TOF, h⁻¹) was also calculated for different crystal types based on oxygen vacancy concentration for MnO₂ (Text S7), As displayed in Fig. S12, the B-MnO₂ showed the highest TOF value of 0.37 h⁻¹, which was 18.5 times as that of the C-MnO₂ (0.02 h⁻¹), indicating that B-MnO₂ has better catalytic performance for CH₃SH.

To gain a deeper insight into the decomposition pathway of CH₃SH, in situ DRIFTS was used to investigate the reaction process at room temperature (30 °C). As displayed in Fig. 6b for B-MnO₂ and Fig. S13b for C-MnO₂, several bands appeared at 2850–3100 cm⁻¹ corresponding to the stretch vibration of C-H [53,66,67], and 1087 cm⁻¹ is assigned to C-S vibrations [68], which are attributed to the adsorbed CH₃S[·] species. However, no bands corresponding to S-H at 2500–2600 cm⁻¹ are observed [69], suggesting that S-H cleavage and the fast adsorption and

transformation of CH₃SH into CH₃SSCH₃. In comparison to the B-MnO₂, it is obvious that the peaks (CH₃S[·] species) were higher and stronger on the C-MnO₂. These results indicated that more CH₃S[·] adsorbed the C-MnO₂ surface rather than through S-S bond binding to form CH₃SSCH₃ during the reaction process, leading to the lower CH₃SSCH₃ formation. The corresponding product results are depicted in Fig. 1e, fewer CH₃SSCH₃ was detected on C-MnO₂ (15 ppm) compared to B-MnO₂ (24 ppm), which revealed that the catalytic reaction is more easily to occur on B-MnO₂ sample (Consistent with DFT results). Besides, the H⁺ generated by the S-H breaking could react with the OH species on the surface to form H₂O (1636 cm⁻¹) [70], the generated adsorption water (H₂O_{ads}) will be activated by oxygen vacancies thus to participate in the reaction. The H₂O_{ads} produced on B-MnO₂ is higher than that of C-MnO₂. And OH species are constantly consumed on B-MnO₂ with the proceed of reaction, while the consumption of OH on C-MnO₂ is lower compared to the B-MnO₂, which further illustrates that the catalytic reaction is more easily occurs on B-MnO₂. Additionally, the sulfur and carbon-containing species are also observed on two catalysts during the CH₃SH reaction (Fig. 6a and Fig. S13a), such as monodentate carbonate species at 1318 cm⁻¹ ($\nu_{as}(COO^-)$), 1471 cm⁻¹ ($\nu_{as}(COO^-)$), and 1506 cm⁻¹ ($\nu_{as}(COO^-)$) [34,68,71], formate species at 1347 cm⁻¹ ($\nu_s(COO^-)$), 1540 cm⁻¹ ($\nu_s(COO^-)$), and 1558 cm⁻¹ ($\nu_s(COO^-)$) [34,53,72,73], and the C=O stretch vibrating bands can be observed at 1653, 1682 and 1698 cm⁻¹ [45,68,71,74]. S-O stretching vibrational at 1059 cm⁻¹ suggested the formation of sulfate species [19,75,76]. These new bands increase with the reaction, representing the breaking of C-S and undergoing further oxidation by ROS, thus converting into SO₄²⁻, COO⁻, and CO₃²⁻ species at room temperature, these results were also confirmed by the IC analysis (Fig. S14). These new bands (COO⁻, CO₃²⁻, and SO₄²⁻) formed on C-MnO₂ are lower than that of B-MnO₂, suggesting the ROS on the surface of B-MnO₂ will gradually oxidize CH₃S[·]. Oxygen vacancies will also activate H₂O_{ads} generated in the reaction process to induce the formation of ROS, implying the better CH₃SH catalytic performance on the B-MnO₂ surface.

In order to study the relationship between the adsorption behavior of CH₃SH and two samples, the DFT calculations were used to compare the adsorption energy of CH₃SH on B-MnO₂ and C-MnO₂. As can be seen from Fig. 6c and d, the adsorption of CH₃SH by two catalysts proceeded through the Mn-S bond, and the adsorption energy of B-MnO₂ is 0.66 eV, which is lower than that of C-MnO₂ (1.10 eV). The stronger interaction between CH₃SH and C-MnO₂ may prevent the release of active species, and escape from catalyst surface, indicating that B-MnO₂ is more prone to adsorb CH₃SH and then proceed the reaction, which can also be proved by the bond length of Mn-O before and after the adsorption of

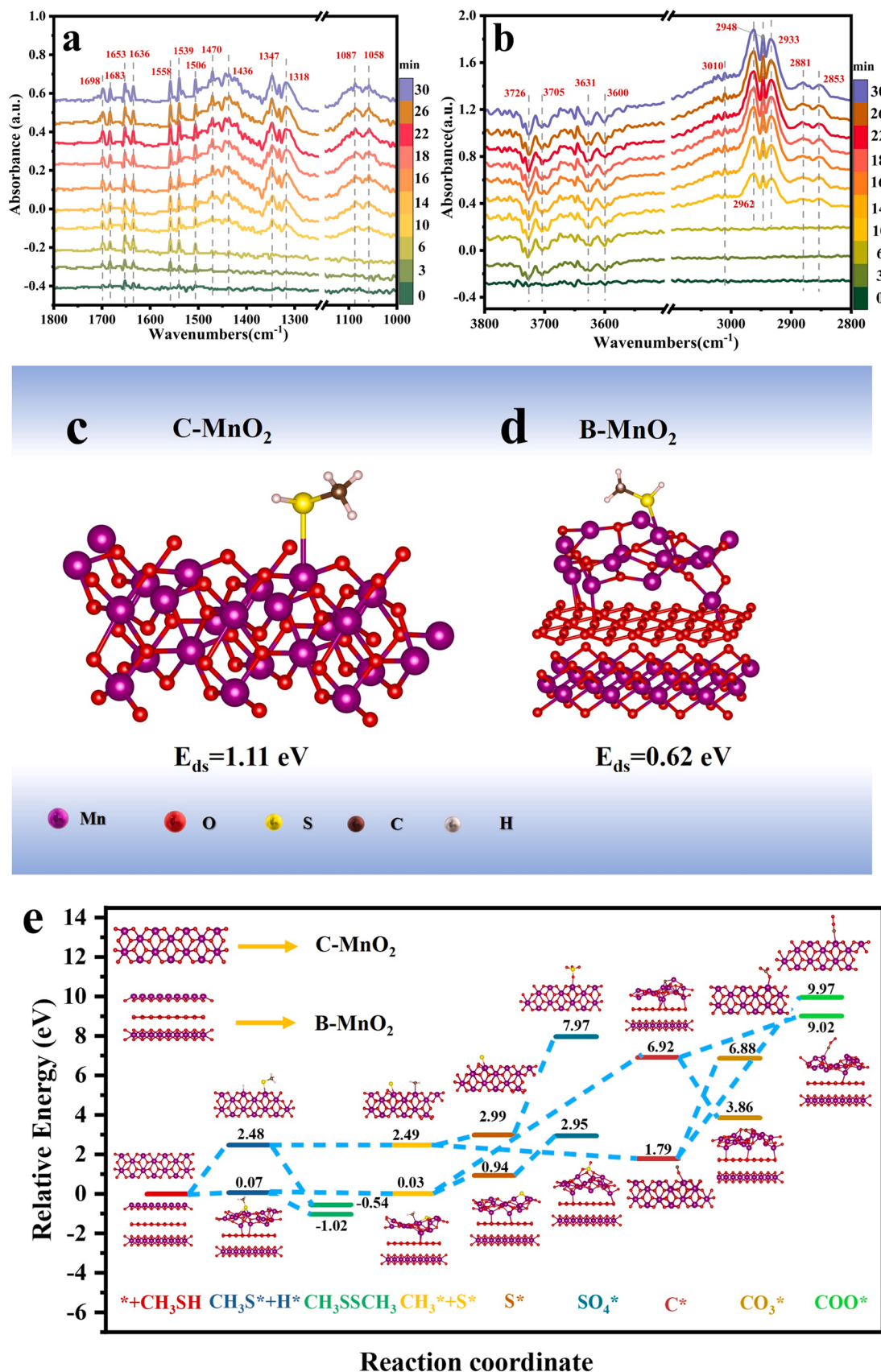


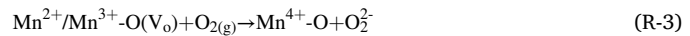
Fig. 6. *In situ* DRIFTS spectra as the function of time on B-MnO₂ (a, b); Optimized adsorption of CH₃SH molecules on B-MnO₂ (c) and C-MnO₂ catalysts (d); Free energy diagram for CH₃SH reaction over the B-MnO₂ and C-MnO₂ catalysts (e).

CH_3SH (Fig. S9). In general, the much lower reaction adsorption energy suggested easier activation of reactants onto the catalyst surface and then react with the surface-active species, hence more intermediate species were detected on the B- MnO_2 surface (Fig. 6a and b). The results of the adsorption energy indicated that the B- MnO_2 samples reacted more readily with CH_3SH than C- MnO_2 , in line with the experimental results and in-situ DRIFTS.

Based on the results of in situ DRIFTS, the energetically favorable reaction pathways of CH_3SH over two catalysts were evaluated by DFT calculations. Besides, the detailed process of the main steps of the CH_3SH decomposition reaction is also vividly depicted in Fig. S15. As shown in Fig. 6e, the intermediates and products of CH_3SH decomposition presented the same results on both of two catalysts, the main difference depends on its difficulty of leading to the CH_3SH conversion. The decomposition of CH_3SH requires breaking of the S-H, C-S and C-H bonds, and a possible pathway of CH_3SH degradation by B- MnO_2 and C- MnO_2 were also proposed. Firstly, it can be seen from in situ DRIFTS (Fig. 6a and b) that CH_3SH is adsorbed and dissociated over the catalyst by breaking the S-H bond to form CH_3S^* and H^* ($\text{CH}_3\text{SH} \rightarrow \text{CH}_3\text{S}^* + \text{H}^*$), while the resulting CH_3S^* group is combined with the S-S bond to generate CH_3SSCH_3 . Secondly, CH_3S^* is broken by the C-S bonds to form CH_3^* and S^* ($\text{CH}_3\text{S}^* \rightarrow \text{CH}_3^* + \text{S}^*$), and CH_3^* is broken by the C-H bonds to produce C^* and H^* ($\text{CH}_3^* \rightarrow \text{C}^* + \text{H}^*$). Finally, the produced S^* and C^* species are oxidized to SO_4^{2-} ($\text{S}^* + \text{O}_2^{2-} / \cdot\text{O}_2 \rightarrow \text{SO}_4^{2-}$), COO^* and CO_3^{2-} ($\text{C}^* + \text{O}_2^{2-} / \cdot\text{O}_2 \rightarrow \text{COO}^* / \text{CO}_3^{2-}$) products. To be specific, the relative energy of CH_3SH decomposed into CH_3S^* and H^* on B- MnO_2 (0.07 eV) is lower than that of C- MnO_2 (2.48 eV), suggesting that B- MnO_2 is more prone to break the S-H bonds, which is consistent with the bond length behavior (Fig. S9) of CH_3SH adsorbed on the two catalysts. Meanwhile, the energy barrier for CH_3SSCH_3 formation through combining CH_3S^* on B- MnO_2 (1.07 eV) is also much lower than C- MnO_2 (3.02 eV), indicating the conversion of CH_3SH to CH_3SSCH_3 occurring more readily on B- MnO_2 , which is consistent with the results of in situ DRIFTS and adsorption energy. It is important to note that, most of the CH_3S^* produced on B- MnO_2 bound to form CH_3SSCH_3 , whereas the CH_3S^* produced on C- MnO_2 mainly adsorbed on the surface of the catalyst and produced lower CH_3SSCH_3 . Next, the C-S broken as well as CH_3SSCH_3 formed by CH_3S^* on the surface, the further dissociation of CH_3S^* into CH_3^* and S^* is exothermic and more favorable on the B- MnO_2 (-0.04 eV) than that of C- MnO_2 (0.01 eV), suggesting that B- MnO_2 is easier to proceed the subsequent reaction. The C-S bonds of the CH_3S^* are broken to form CH_3^* and S^* ($\text{CH}_3\text{S}^* \rightarrow \text{CH}_3^* + \text{S}^*$), then S^* will be oxidized by ROS to generate SO_4^{2-} , and it can also be seen that the energy barrier for generating SO_4^{2-} on B- MnO_2 (2.01 eV) is much lower than on C- MnO_2 (4.98 eV), implying the sulfur species on the surface of B- MnO_2 are more easily oxidized. Besides, CH_3^* will break through C-H to form C^* and H^* , and the C^* energy barrier for C-H bond breakage formation in B- MnO_2 was as high as 6.89 eV, indicating that the break of C-H is the rate-determining step of B- MnO_2 . Therefore, ROS can oxidize the C^* species to COO^* and CO_3^{2-} ($\text{C}^* + \text{O}_2^{2-} / \cdot\text{O}_2 \rightarrow \text{COO}^* / \text{CO}_3^{2-}$). On the contrary, compared to the energy barrier for CO_3^{2-} formation from C^* on C- MnO_2 (5.09 eV), the generation of CO_3^{2-} requires the exothermic energy of -3.06 eV on B- MnO_2 , implying that CO_3^{2-} formation is more likely occur on B- MnO_2 than C- MnO_2 . And the energy barrier for the formation of COO^* on B- MnO_2 (2.1 eV) is also lower than C- MnO_2 (8.18 eV), suggesting that the generation of carbon-containing species are the rate-determining step on C- MnO_2 , which is more likely to present on the B- MnO_2 surface in the form of oxidation state. Logically, the production of SO_4^{2-} , CO_3^{2-} and COO^* on C- MnO_2 is smaller than that of B- MnO_2 surface, which can be testified from the in-situ DRIFTS (Fig. S13a). The above results prove that B- MnO_2 sample is more likely to catalyze the reaction with CH_3SH to generate CH_3SSCH_3 and sulfur and carbon-containing species. Notably, although these reactions processes require high energy and are generally challenging to occur, and we also detected large amounts of intermediates at room temperature by in situ DRIFTS, indicating that the occurrence of ROS on the catalyst surface

which can induce the formation of these products at room temperature. In order to furthering investigate the possible intermediate species, the GC-MS experiment were carried out and only CH_3SSCH_3 can be detect, in addition, we also increase the concentration of CH_3SH to 5000 ppm, and there is only little SO_2 can be detected (Fig. S16).

Based on the above analysis, the possible decomposition pathways for CH_3SH over the two catalysts include sequential steps. Firstly, CH_3SH was transformed to CH_3S^* through the cleavage of S-H bonds and the formation of CH_3SSCH_3 by coupling CH_3S^* (R-1 and R-2). Secondly, oxygen molecules can be activated by the oxygen vacancies (O_v) to form into ROS (O_2^{2-}), and quickly transformed into $\cdot\text{O}_2 / \cdot\text{OH}$ through a chain cycle reaction (R-3 and R-4). Afterwards, the O_v can be regenerated by a cycle reaction to favor the highly efficient catalytic of CH_3SH (R-5). Hence, the C-S bonds continue to be attacked by ROS and to produce SO_4^{2-} on the surface of the catalyst (R-63 and R-7). Finally, the broken C-H bonds are also oxidized by ROS to COO^* and CO_3^{2-} (R-8 and R-9) (Scheme 1). Besides, the A- MnO_2 catalyst was analyzed by XRD, SEM and TEM (Fig. S17), these results proved that the A- MnO_2 is also amorphous catalyst. Furthermore, the oxygen species and ROS were also investigated by O_2 -TPD and EPR (Fig. S18), these results clearly showed that A- MnO_2 can produce ROS and display better catalytic performance towards to CH_3SH , which is very similar to the performance of B- MnO_2 .



3.5. Implications for controlling environmental odor pollutants

In order to test the universality of the B- MnO_2 sample for other typical S-VOCs ($\text{C}_2\text{H}_5\text{SH}$, $\text{C}_3\text{H}_7\text{SH}$, mixed CH_3SH and $\text{C}_2\text{H}_5\text{SH}$, mixed CH_3SH and $\text{C}_3\text{H}_7\text{SH}$), the catalytic activities of the various S-VOCs were also explored, which can evaluate the commercial potential for the catalytic decomposition of S-VOCs on a large-scale practical application. As shown in Fig. 7a and b, the removal efficiency of $\text{C}_2\text{H}_5\text{SH}$, and $\text{C}_3\text{H}_7\text{SH}$ can achieved 100% conversion in the range of 30 – 400 °C. Meanwhile, the catalytic activity under mixed mercaptans (mixed CH_3SH and $\text{C}_2\text{H}_5\text{SH}$, mixed CH_3SH and $\text{C}_3\text{H}_7\text{SH}$) is also examined on B- MnO_2 (Fig. 7c and d). Under the condition of mixed mercaptans, both of them can obtain 100% conversion at room temperature, and showing very excellent catalytic performance towards to various S-VOCs. Subsequently, the stability test of mixed mercaptans was also explored. Fig. 7e shows the stability of the mix of CH_3SH and $\text{CH}_3\text{CH}_2\text{SH}$, their removal efficiency can achieve 100% within 24 h at room temperature both in mixed CH_3SH and $\text{CH}_3\text{CH}_2\text{SH}$. As shown in Fig. 7f, the stability of mixing CH_3SH with $\text{CH}_3\text{CH}_2\text{CH}_2\text{SH}$ is also performed, and the conversion of CH_3SH with $\text{CH}_3\text{CH}_2\text{CH}_2\text{SH}$ in the gas mixture reached 100% for about 39 h at 30 °C. In addition, for B- MnO_2 , high concentrations of CH_3SH can be also completely converted at room temperature, and the more details about products from B- MnO_2 and C- MnO_2 are also given in the Fig. S19, S20 and Text S8, S9. It can be concluded from the above experiments that the B- MnO_2 catalyst is universal in the removal of S-VOCs both in low (100 ppm) and high (5000 ppm) concentrations,

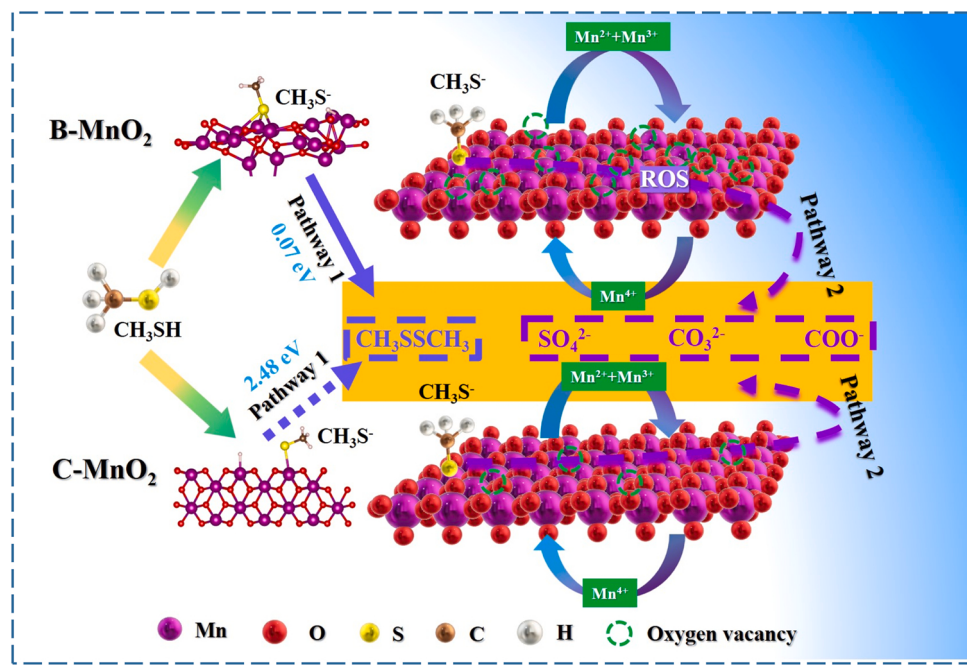
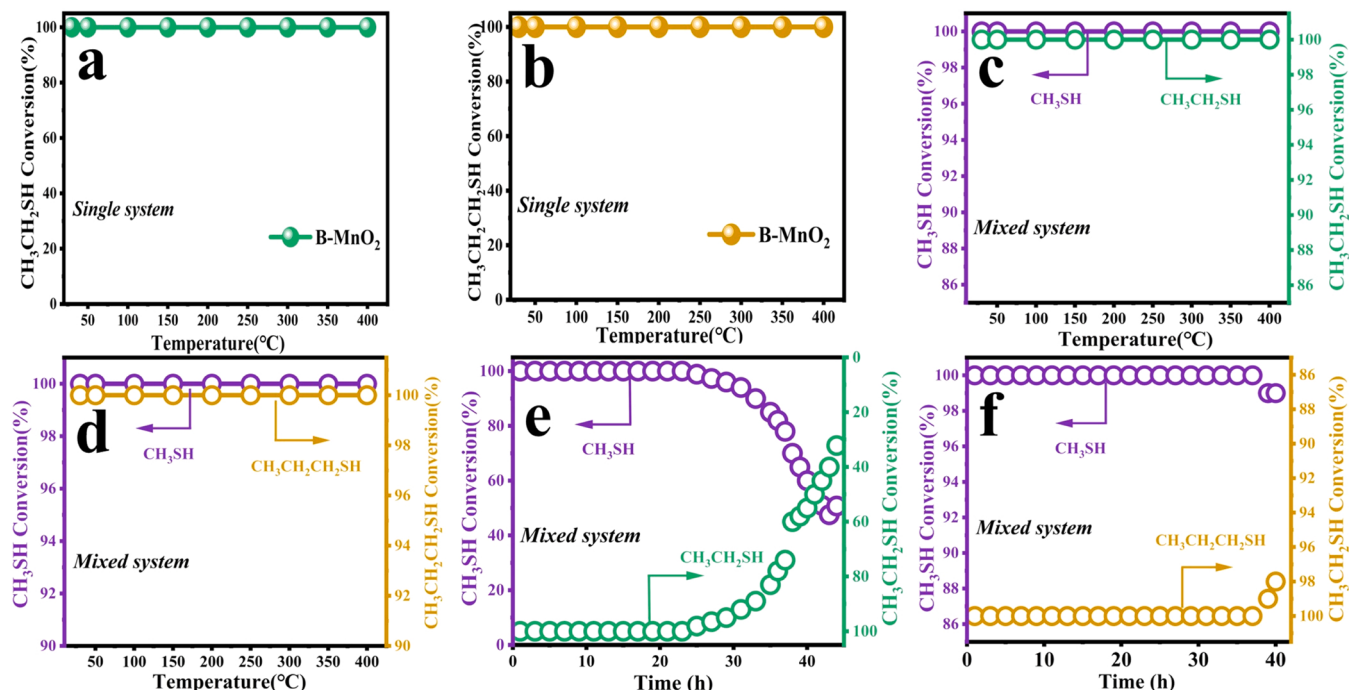
Scheme 1. Reaction mechanisms for CH_3SH decomposition with various MnO_2 samples.

Fig. 7. The catalytic activities of $\text{CH}_3\text{CH}_2\text{SH}$ (a) and $\text{CH}_3\text{CH}_2\text{CH}_2\text{SH}$ (b) on B-MnO_2 ; The catalytic activities of mixture CH_3SH and $\text{CH}_3\text{CH}_2\text{SH}$ on B-MnO_2 (c); The catalytic activities of mixture CH_3SH and $\text{CH}_3\text{CH}_2\text{CH}_2\text{SH}$ on B-MnO_2 (d); The stability test of mixture CH_3SH and $\text{CH}_3\text{CH}_2\text{SH}$ on B-MnO_2 (e); The stability test of mixture CH_3SH and $\text{CH}_3\text{CH}_2\text{CH}_2\text{SH}$ on B-MnO_2 (f).

which makes it own a broader application perspective.

4. Conclusions

Amorphous MnO_2 catalysts are promising candidates for future generation S-VOCs degradation catalysts because of numerous advantages such as low operation cost, excellent catalytic properties under low temperature, and facile fabrication engineering. This work firstly revealed that the CH_3SH , $\text{C}_2\text{H}_5\text{SH}$, $\text{C}_3\text{H}_7\text{SH}$ and mixed multi-component

mercaptans could be eliminated from ambient air by amorphous MnO_2 at room temperatures. The results offered new insightful information for understanding the role of MnO_2 and provided novel mechanistic knowledge for the abatement of typical S-VOCs. Moreover, the results from this study also demonstrated the catalysts are easily prepared and inexpensive, which can be developed for the catalytic decomposition of S-VOCs on a large scale practical applications, making the process more conducive to eliminating odorous gases like S-VOCs compared to previous methods requiring high operation temperature or additives [17].

[19]. The durability of the excellent catalysts will also need to be further evaluated as the function of time in the future, but preliminary tests have indicated that the catalysts own high stability. Thus, this work can provide in-depth insights into the developing novel and efficient technology to control atmospheric odor pollutants like S-VOCs and other VOCs at room temperature both for the actual industrial application and real environment in the future.

CRediT authorship contribution statement

Jiangping Liu: Experimental design, Writing-original draft, Writing-review&editing. **Hong Su:** Performed the laboratory experiments, Data curation. **Yanan Hu:** Data curation, Writing-review&editing. **Chenhai Gong:** Performed the laboratory experiments. **Jichang Lu:** Formal analysis. **Dedong He:** Formal analysis. **Wenjie Zhu:** Formal analysis. **Dingkai Chen:** Formal analysis. **Xiaohua Cao:** Formal analysis. **Jun Li:** DFT analysis. **Sasho Gligorovski:** Review of the manuscript, Resources. **Yongming Luo:** Review of the manuscript, Resources.

Declaration of Competing Interest

The authors declare that they have no known competing financial interests or personal relationships that could have appeared to influence the work reported in this paper.

Data Availability

Data will be made available on request.

Acknowledgments

This work was supported by National Natural Science Foundation of China (No. 42030712, 42207127, 21966018, 22166021) Key Project of Natural Science Foundation of Yunnan Province (Grant No. 202101AS070026) and Applied Basic Research Foundation of Yunnan Province (Grant No. 202101BE070001-027, 2022J0069 and 202105AE160019).

Appendix A. Supporting information

Supplementary data associated with this article can be found in the online version at [doi:10.1016/j.apcatb.2023.122877](https://doi.org/10.1016/j.apcatb.2023.122877).

References

- [1] D. Gu, A.B. Guenther, J.E. Shilling, H. Yu, M. Huang, C. Zhao, Q. Yang, S.T. Martin, P. Artaxo, S. Kim, R. Seco, T. Stavrakou, K.M. Longo, J. Tóta, R.A.F. de Souza, O. Vega, Y. Liu, M. Shrivastava, E.G. Alves, F.C. Santos, G. Leng, Z. Hu, Airborne observations reveal elevational gradient in tropical forest isoprene emissions, *Nat. Commun.* 8 (1) (2017) 15541, <https://doi.org/10.1038/ncomms15541>.
- [2] G. Arney, S.D. Domagal Goldman, V.S. Meadows, Organic haze as a biosignature in anoxic Earth-like atmospheres, *Astrobiology* 18 (3) (2018) 311–329. (<https://arxiv.org/abs/1711.01675>).
- [3] C. He, S.M. Hörst, N.K. Lewis, X. Yu, J.I. Moses, P. McGuiggan, M.S. Marley, E.M. R. Kempton, S.E. Moran, C.V. Morley, V. Vuitton, Sulfur-driven haze formation in warm CO₂-rich exoplanet atmospheres, *Nat. Astron.* 4 (10) (2020) 986–993, <https://doi.org/10.1038/s41550-020-1072-9>.
- [4] G. Muthuraman, S.J. Chung, I.S. Moon, The combined removal of methyl mercaptan and hydrogen sulfide via an electro-reactor process using a low concentration of continuously regenerable Ag(II) active catalyst, *J. Hazard. Mater.* 193 (2011) 257–263, <https://doi.org/10.1016/j.jhazmat.2011.07.054>.
- [5] J.R. Kastner, K.C. Das, Q. Buquoi, N.D. Melear, Low temperature catalytic oxidation of hydrogen sulfide and methanethiol using wood and coal fly ash, *Environ. Sci. Technol.* 37 (11) (2003) 2568–2574, <https://doi.org/10.1021/es0259988>.
- [6] E. Huguet, B. Coq, R. Durand, C. Leroi, R. Cadours, V. Hulea, A highly efficient process for transforming methyl mercaptan into hydrocarbons and H₂S on solid acid catalysts, *Appl. Catal. B Environ.* 134–135 (2013) 344–348, <https://doi.org/10.1016/j.apcatb.2013.01.037>.
- [7] N. Laosiripojana, S. Assabumrungrat, Conversion of poisonous methanethiol to hydrogen-rich gas by chemisorption/reforming over nano-scale CeO₂: The use of CeO₂ as catalyst coating material, *Appl. Catal. B Environ.* 102 (1) (2011) 267–275, <https://doi.org/10.1016/j.apcatb.2010.12.008>.
- [8] D. He, H. Hao, D. Chen, J. Liu, J. Yu, J. Lu, F. Liu, S. He, K. Li, Y. Luo, Effects of rare-earth (Nd, Er and Y) doping on catalytic performance of HZSM-5 zeolite catalysts for methyl mercaptan (CH₃SH) decomposition, *Appl. Catal. A Gen.* 533 (2017) 66–74, <https://doi.org/10.1016/j.apcata.2017.01.011>.
- [9] J. Liu, D. He, D. Chen, H. Hao, J. Yu, J. Lu, F. Liu, P. Liu, Y. Zhao, Y. Luo, Promotional effects of rare-earth (La, Ce and Pr) modification over HZSM-5 for methyl mercaptan catalytic decomposition, *J. Taiwan Inst. Chem. Eng.* 80 (2017) 262–268, <https://doi.org/10.1016/j.jtice.2017.07.006>.
- [10] D. He, Y. Zhao, S. Yang, Y. Mei, J. Yu, J. Liu, D. Chen, S. He, Y. Luo, Enhancement of catalytic performance and resistance to carbonaceous deposit of lanthanum (La) doped HZSM-5 catalysts for decomposition of methyl mercaptan, *Chem. Eng. J.* 336 (2018) 579–586, <https://doi.org/10.1016/j.cej.2017.12.054>.
- [11] D. He, G. Wan, H. Hao, D. Chen, J. Lu, L. Zhang, F. Liu, L. Zhong, S. He, Y. Luo, Microwave-assisted rapid synthesis of CeO₂ nanoparticles and its desulfurization processes for CH₃SH catalytic decomposition, *Chem. Eng. J.* 289 (2016) 161–169, <https://doi.org/10.1016/j.cej.2015.12.103>.
- [12] D. He, L. Zhang, Y. Zhao, Y. Mei, D. Chen, S. He, Y. Luo, Recycling spent Cr adsorbents as catalyst for eliminating methylmercaptan, *Environ. Sci. Technol.* 52 (6) (2018) 3669–3675, <https://doi.org/10.1021/acs.est.7b06357>.
- [13] Y. Zhao, D. Chen, J. Liu, D. He, X. Cao, C. Han, J. Lu, Y. Luo, Tuning the metal-support interaction on chromium-based catalysts for catalytically eliminate methyl mercaptan: anchored active chromium species through surface hydroxyl groups, *Chem. Eng. J.* 389 (2020), 124384, <https://doi.org/10.1016/j.cej.2020.124384>.
- [14] F. Tian, H. Li, M. Zhu, W. Tu, D. Lin, Y. Han, Effect of MnO₂ polymorphs' structure on low-temperature catalytic oxidation: crystalline controlled oxygen vacancy formation, *ACS Appl. Mater. Inter.* 14 (16) (2022) 18525–18538, <https://doi.org/10.1021/acsm.2c01727>.
- [15] J. Huang, S. Zhong, Y. Dai, C.-C. Liu, H. Zhang, Effect of MnO₂ phase structure on the oxidative reactivity toward bisphenol A degradation, *Environ. Sci. Technol.* 52 (19) (2018) 11309–11318, <https://doi.org/10.1021/acs.est.8b03383>.
- [16] D. Xia, W. Xu, Y. Wang, J. Yang, Y. Huang, L. Hu, C. He, D. Shu, D.Y.C. Leung, Z. Pang, Enhanced performance and conversion pathway for catalytic ozonation of methyl mercaptan on single-atom Ag deposited three-dimensional ordered mesoporous MnO₂, *Environ. Sci. Technol.* 52 (22) (2018) 13399–13409, <https://doi.org/10.1021/acs.est.8b03696>.
- [17] C. He, Y. Wang, Z. Li, Y. Huang, Y. Liao, D. Xia, S. Lee, Facet engineered α -MnO₂ for efficient catalytic ozonation of odor CH₃SH: oxygen vacancy-induced active centers and catalytic mechanism, *Environ. Sci. Technol.* 54 (19) (2020) 12771–12783, <https://doi.org/10.1021/acs.est.0c05235>.
- [18] D. Ma, W. Liu, Y. Huang, D. Xia, Q. Lian, C. He, Enhanced catalytic ozonation for eliminating CH₃SH via stable and circular electronic metal-support interactions of Si-O-Mn bonds with low Mn loading, *Environ. Sci. Technol.* 56 (6) (2022) 3678–3688, <https://doi.org/10.1021/acs.est.1c07065>.
- [19] C. He, Y. Liao, C. Chen, D. Xia, Y. Wang, S. Tian, J. Yang, D. Shu, Realizing a redox-robust Ag/MnO₂ catalyst for efficient wet catalytic ozonation of S-VOCs: Promotional role of Ag(0)/Ag(I)-Mn based redox shuttle, *Appl. Catal. B Environ.* 303 (2022), 120881, <https://doi.org/10.1016/j.apcatb.2021.120881>.
- [20] W. Yang, Y. Zhu, F. You, L. Yan, Y. Ma, C. Lu, P. Gao, Q. Hao, W. Li, Insights into the surface-defect dependence of molecular oxygen activation over birnessite-type MnO₂, *Appl. Catal. B* 233 (2018) 184–193, <https://doi.org/10.1016/j.apcatb.2018.03.107>.
- [21] J. Zeng, H. Xie, Z. Liu, X. Liu, G. Zhou, Y. Jiang, Oxygen vacancy induced MnO₂ catalysts for efficient toluene catalytic oxidation, *Catal. Sci. Technol.* 11 (20) (2021) 6708–6723, <https://doi.org/10.1039/D1CY01274F>.
- [22] M. Ruiz García, M. Villalobos, A. Voegelin, T. Pi Puig, N. Martínez Villegas, J. Göttlicher, Transformation of hexagonal birnessite upon reaction with thallium (I): Effects of birnessite crystallinity, pH, and thallium concentration, *Environ. Sci. Technol.* 55 (8) (2021) 4862–4870, <https://doi.org/10.1021/acs.est.0c07886>.
- [23] K. Zeng, Y. Wang, C. Huang, H. Liu, X. Liu, Z. Wang, J. Yu, C. Zhang, Catalytic combustion of propane over MnNbO_x composite oxides: the promotional role of niobium, *Ind. Eng. Chem. Res.* 60 (17) (2021) 6111–6120, <https://doi.org/10.1021/acs.iecr.1c00699>.
- [24] B. Zhang, J. Ji, B. Liu, D. Zhang, S. Liu, H. Huang, Highly efficient ozone decomposition against harsh environments over long-term stable amorphous MnO_x catalysts, *Appl. Catal. B Environ.* 315 (2022), 121552.
- [25] Y. Shen, J. Deng, X. Hu, X. Chen, H. Yang, D. Cheng, D. Zhang, Expediting toluene combustion by harmonizing the Ce-O strength over Co-doped CeZr oxide catalysts, *Environ. Sci. Technol.* 57 (4) (2023) 1797–1806, <https://doi.org/10.1021/acs.est.2c07853>.
- [26] Y. Shen, J. Deng, L. Han, W. Ren, D. Zhang, Low-temperature combustion of toluene over Cu-doped SmMn₂O₅ mullite catalysts via creating highly active Cu²⁺-O-Mn⁴⁺ sites, *Environ. Sci. Technol.* 56 (14) (2022) 10433–10441, <https://doi.org/10.1021/acs.est.2c02866>.
- [27] Y. Shen, J. Deng, S. Impeng, S. Li, T. Yan, J. Zhang, L. Shi, D. Zhang, *Environ. Sci. Technol.* 54 (16) (2020) 10342–10350, <https://doi.org/10.1021/acs.est.0c02680>.
- [28] H. Zhang, S. Sui, X. Zheng, R. Cao, P. Zhang, One-pot synthesis of atomically dispersed Pt on MnO₂ for efficient catalytic decomposition of toluene at low temperatures, *Appl. Catal. B Environ.* 257 (2019), 117878, <https://doi.org/10.1016/j.apcatb.2019.117878>.
- [29] G. Kresse, J. Furthmüller, Efficiency of ab initio total energy calculations for metals and semiconductors using a plane-wave basis set, *Comput. Mater. Sci.* 6 (1) (1996) 15–50, [https://doi.org/10.1016/0927-0256\(96\)00008-0](https://doi.org/10.1016/0927-0256(96)00008-0).

[30] G. Kresse, J. Furthmüller, Efficient iterative schemes for ab initio total-energy calculations using a plane-wave basis set, Phys. Rev. B 54 (16) (1996) 11169, <https://doi.org/10.1103/physrevb.54.11169>.

[31] J.P. Perdew, K. Burke, M. Ernzerhof, Generalized gradient approximation made simple, Phys. Rev. Lett. 77 (18) (1996) 3865, <https://doi.org/10.1103/PhysRevLett.77.3865>.

[32] G. Kresse, D. Joubert, From ultrasoft pseudopotentials to the projector augmented-wave method, Phys. Rev. B 59 (3) (1999) 1758, <https://doi.org/10.1103/physrevb.59.1758>.

[33] P.E. Blöchl, Projector augmented-wave method, Phys. Rev. B 50 (24) (1994) 17953, <https://doi.org/10.1103/physrevb.50.17953>.

[34] J. Wang, P. Zhang, J. Li, C. Jiang, R. Yunus, J. Kim, Room-temperature oxidation of formaldehyde by layered manganese oxide: effect of water, Environ. Sci. Technol. 49 (20) (2015) 12372–12379, <https://doi.org/10.1021/acs.est.5b02085>.

[35] B. Bai, Q. Qiao, H. Arandiyani, J. Li, J. Hao, Three-dimensional ordered mesoporous MnO₂-supported Ag nanoparticles for catalytic removal of formaldehyde, Environ. Sci. Technol. 50 (5) (2016) 2635–2640, <https://doi.org/10.1021/acs.est.5b03342>.

[36] H. Zhang, X. Zheng, T. Xu, P. Zhang, Atomically dispersed Y or La on birnessite-type MnO₂ for the catalytic decomposition of low-concentration toluene at room temperature, ACS Appl. Mater. Inter. 13 (15) (2021) 17532–17542, <https://doi.org/10.1021/acsmami.1c01433>.

[37] C. Shan, Y. Zhang, Q. Zhao, K. Fu, Y. Zheng, R. Han, C. Liu, N. Ji, W. Wang, Q. Liu, Acid etching-induced *in situ* growth of λ -MnO₂ over CoMn spinel for low-temperature volatile organic compound oxidation, Environ. Sci. Technol. 56 (14) (2022) 10381–10390, <https://doi.org/10.1021/acs.est.2c02483>.

[38] G. Chen, D. Hong, H. Xia, W. Sun, S. Shao, B. Gong, S. Wang, J. Wu, X. Wang, Q. Dai, Amorphous and homogeneously Zr-doped MnO_x with enhanced acid and redox properties for catalytic oxidation of 1,2-Dichloroethane, Chem. Eng. J. 428 (2022), 131067, <https://doi.org/10.1016/j.cej.2021.131067>.

[39] S. Rong, P. Zhang, F. Liu, Y. Yang, Engineering crystal facet of α -MnO₂ nanowire for highly efficient catalytic oxidation of carcinogenic airborne formaldehyde, ACS Catal. 8 (4) (2018) 3435–3446, <https://doi.org/10.1021/acscatal.8b00456>.

[40] S. Zhu, Z. Zhou, D. Zhang, H. Wang, Synthesis of mesoporous amorphous MnO₂ from SBA-15 via surface modification and ultrasonic waves, Microporous Mesoporous Mater. 95 (1) (2006) 257–264, <https://doi.org/10.1016/j.micromeso.2006.05.029>.

[41] S. Rong, K. Li, P. Zhang, F. Liu, J. Zhang, Potassium associated manganese vacancy in birnessite-type manganese dioxide for airborne formaldehyde oxidation, Catal. Sci. Technol. 8 (7) (2018) 1799–1812, <https://doi.org/10.1039/C7CY02121F>.

[42] D. Ding, Y. Zhou, T. He, S. Rong, Facet selectively exposed α -MnO₂ for complete photocatalytic oxidation of carcinogenic HCHO at ambient temperature, Chem. Eng. J. 431 (2022), 133737, <https://doi.org/10.1016/j.cej.2021.133737>.

[43] Q. Li, X. Huang, G. Su, M. Zheng, C. Huang, M. Wang, C. Ma, D. Wei, The regular-persistent free radicals and associated reaction mechanism for the degradation of 1,2,4-Trichlorobenzene over different MnO₂ polymorphs, Environ. Sci. Technol. 52 (22) (2018) 13351–13360, <https://doi.org/10.1021/acs.est.8b03789>.

[44] W. Yang, Z. Su, Z. Xu, W. Yang, Y. Peng, J. Li, Comparative study of α -, β -, γ - and δ -MnO₂ on toluene oxidation: Oxygen vacancies and reaction intermediates, Appl. Catal. B Environ. 260 (2020), 118150, <https://doi.org/10.1016/j.apcatb.2019.118150>.

[45] X. Zheng, G. Zhang, Z. Yao, Y. Zheng, L. Shen, F. Liu, Y. Cao, S. Liang, Y. Xiao, L. Jiang, Engineering of crystal phase over porous MnO₂ with 3D morphology for highly efficient elimination of H₂S, J. Hazard. Mater. 411 (2021), 125180, <https://doi.org/10.1016/j.jhazmat.2021.125180>.

[46] X. Fang, Y. Liu, Y. Cheng, W. Cen, Mechanism of Ce-modified birnessite-MnO₂ in promoting SO₂ poisoning resistance for low-temperature NH₃-SCR, ACS Catal. 11 (7) (2021) 4125–4135, <https://doi.org/10.1021/acscatal.0c05697>.

[47] B. Chen, B. Wu, L. Yu, M. Crocker, C. Shi, Investigation into the catalytic roles of various oxygen species over different crystal phases of MnO₂ for C₆H₆ and HCHO oxidation, ACS Catal. 10 (11) (2020) 6176–6187, <https://doi.org/10.1021/acscatal.0c00459>.

[48] X. Li, J. Ma, L. Yang, G. He, C. Zhang, R. Zhang, H. He, Oxygen vacancies induced by transition metal doping in γ -MnO₂ for highly efficient ozone decomposition, Environ. Sci. Technol. 52 (21) (2018) 12685–12696, <https://doi.org/10.1021/acs.est.8b04294>.

[49] G. Zhu, J. Zhu, W. Li, W. Yao, R. Zong, Y. Zhu, Q. Zhang, Tuning the K⁺ concentration in the tunnels of α -MnO₂ to increase the content of oxygen vacancy for ozone elimination, Environ. Sci. Technol. 52 (15) (2018) 8684–8692, <https://doi.org/10.1021/acs.est.8b01594>.

[50] B. Bai, J. Li, J. Hao, 1D-MnO₂, 2D-MnO₂ and 3D-MnO₂ for low-temperature oxidation of ethanol, Appl. Catal., B 164 (2015) 241–250, <https://doi.org/10.1016/j.apcatb.2014.08.044>.

[51] R. Cao, L. Li, P. Zhang, L. Gao, S. Rong, Regulating oxygen vacancies in ultrathin δ -MnO₂ nanosheets with superior activity for gaseous ozone decomposition, Environ. Sci. Nano 8 (6) (2021) 1628–1641, <https://doi.org/10.1039/DEN00149C>.

[52] R. Yang, Z. Guo, L. Cai, R. Zhu, Y. Fan, Y. Zhang, P. Han, W. Zhang, X. Zhu, Q. Zhao, Z. Zhu, C.K. Chan, Z. Zeng, Investigation into the phase-activity relationship of MnO₂ nanomaterials toward ozone-assisted catalytic oxidation of toluene, Small 17 (50) (2021) 2103052, <https://doi.org/10.1002/smll.202103052>.

[53] H. Sun, Z. Liu, S. Chen, X. Quan, The role of lattice oxygen on the activity and selectivity of the OMS-2 catalyst for the total oxidation of toluene, Chem. Eng. J. 270 (2015) 58–65, <https://doi.org/10.1016/j.cej.2015.02.017>.

[54] Y. Zheng, W. Wang, D. Jiang, L. Zhang, Amorphous MnO_x modified Co₃O₄ for formaldehyde oxidation: improved low-temperature catalytic and photothermocatalytic activity, Chem. Eng. J. 284 (2016) 21–27, <https://doi.org/10.1016/j.cej.2015.08.137>.

[55] H. Wang, S. Chen, D. Yong, X. Zhang, S. Li, W. Shao, X. Sun, B. Pan, Y. Xie, Giant electron-hole interactions in confined layered structures for molecular oxygen activation, J. Am. Chem. Soc. 139 (13) (2017) 4737–4742, <https://doi.org/10.1021/jacs.6b12273>.

[56] R. Li, Y. Weng, X. Zhou, X. Wang, Y. Mi, R. Chong, H. Han, C. Li, Achieving overall water splitting using titanium dioxide-based photocatalysts of different phases, Energy Environ. Sci. 8 (8) (2015) 2377–2382, <https://doi.org/10.1039/CSE01398D>.

[57] H. Li, H. Shang, Y. Li, X. Cao, Z. Yang, Z. Ai, L. Zhang, Interfacial charging-decharging strategy for efficient and selective aerobic NO oxidation on oxygen vacancy, Environ. Sci. Technol. 53 (12) (2019) 6964–6971, <https://doi.org/10.1021/acs.est.9b01287>.

[58] X. Zhang, C. Pei, X. Chang, S. Chen, R. Liu, Z. Zhao, R. Mu, J. Gong, FeO₆ octahedral distortion activates lattice oxygen in perovskite ferrite for methane partial oxidation coupled with CO₂ splitting, J. Am. Chem. Soc. 142 (26) (2020) 11540–11549, <https://doi.org/10.1021/jacs.0c04643>.

[59] X. Wan, L. Wang, S. Zhang, H. Shi, J. Niu, G. Wang, W. Li, D. Chen, H. Zhang, X. Zhou, W. Wang, Ozono decomposition below room temperature using Mn-based multilite YMn₂O₅, Environ. Sci. Technol. 56 (12) (2022) 8746–8755, <https://doi.org/10.1021/acs.est.1c08922>.

[60] B. Zhang, L. Zhou, M. Qi, Z. Li, J. Han, K. Li, Y. Zhang, F. Dehghani, R. Liu, J. Yun, Outstanding stability and enhanced catalytic activity for toluene oxidation by Si-O-Mn interaction over MnO_x/SiO₂, Ind. Eng. Chem. Res. 61 (2) (2022) 1044–1055, <https://doi.org/10.1021/acs.iecr.1c02504>.

[61] J. Wang, J. Li, C. Jiang, P. Zhou, P. Zhang, J. Yu, The effect of manganese vacancy in birnessite-type MnO₂ on room-temperature oxidation of formaldehyde in air, Appl. Catal. B Environ. 204 (2017) 147–155, <https://doi.org/10.1016/j.apcatb.2016.11.036>.

[62] J.S. Yoo, X. Rong, Y. Liu, A.M. Kolpak, Role of lattice oxygen participation in understanding trends in the oxygen evolution reaction on perovskites, ACS Catal. 8 (5) (2018) 4628–4636, <https://doi.org/10.1021/acscatal.8b00612>.

[63] S. Kaiser, F. Maleki, K. Zhang, W. Harbich, U. Heiz, S. Tosoni, B.A.J. Lechner, G. Pacchioni, F. Esch, Cluster catalysis with lattice oxygen: Tracing oxygen transport from a magnetite (001) support onto small Pt clusters, ACS Catal. 11 (15) (2021) 9519–9529, <https://doi.org/10.1021/acscatal.1c01451>.

[64] C. Wang, Z. Han, X. Zou, H. Liu, H. Wang, D. Shu, T. Chen, S.L. Suib, Ultrathin MnO₂-coated FeOOH catalyst for indoor formaldehyde oxidation at ambient temperature: New insight into surface reactive oxygen species and in-field testing in an air cleaner, Environ. Sci. Technol. 56 (15) (2022) 10963–10976, <https://doi.org/10.1021/acs.est.2c02663>.

[65] Q. Tang, L. Jiang, J. Liu, S. Wang, G. Sun, Effect of surface manganese valence of manganese oxides on the activity of the oxygen reduction reaction in alkaline media, ACS Catal. 4 (2) (2014) 457–463, <https://doi.org/10.1021/cs400938s>.

[66] C. Zhang, F. Liu, Y. Zhai, H. Ariga, N. Yi, Y. Liu, K. Asakura, M. Flytzani Stephanopoulos, H. He, Alkali-metal-promoted Pt/TiO₂ opens a more efficient pathway to formaldehyde oxidation at ambient temperatures, Angew. Chem. Int. Ed. 51 (38) (2012) 9628–9632, <https://doi.org/10.1002/anie.201202034>.

[67] J. Quiroz, J. Giraudon, A. Gervasini, C. Dujardin, C. Lancelot, M. Trentesaux, J. Lamontier, Total oxidation of formaldehyde over MnO_x-CeO₂ catalysts: The effect of acid treatment, ACS Catal. 5 (4) (2015) 2260–2269, <https://doi.org/10.1021/cs501879j>.

[68] T.J. Toops, M. Crocker, New sulfur adsorbents derived from layered double hydroxides: II. DRIFTS study of COS and H₂S adsorption, Appl. Catal. B Environ. 82 (3) (2008) 199–207, <https://doi.org/10.1016/j.apcatb.2008.01.013>.

[69] Y. Huang, D. Ma, W. Liu, D. Xia, L. Hu, J. Yang, P. Liao, C. He, Enhanced catalytic ozonation for eliminating CH₃S via graphene-supported positively charged atomic Pt undergoing Pt²⁺/Pt⁴⁺ redox cycle, Environ. Sci. Technol. 55 (24) (2021) 16723–16734, <https://doi.org/10.1021/acs.est.1c06938>.

[70] H. Gu, J. Lan, Y. Liu, C. Ling, K. Wei, G. Zhan, F. Guo, F. Jia, Z. Ai, L. Zhang, X. Liu, Water enables lattice oxygen activation of transition metal oxides for volatile organic compound oxidation, ACS Catal. 12 (18) (2022) 11272–11280, <https://doi.org/10.1021/acscatal.2e03552>.

[71] L. Zhu, J. Wang, S. Rong, H. Wang, P. Zhang, Cerium modified birnessite-type MnO₂ for gaseous formaldehyde oxidation at low temperature, Appl. Catal. B Environ. 211 (2017) 212–221, <https://doi.org/10.1016/j.apcatb.2017.04.025>.

[72] J. Wang, J. Li, P. Zhang, G. Zhang, Understanding the “seesaw effect” of interlayered K⁺ with different structure in manganese oxides for the enhanced formaldehyde oxidation, Appl. Catal. B Environ. 224 (2018) 863–870, <https://doi.org/10.1016/j.apcatb.2017.11.019>.

[73] C. Shi, B. Chen, X. Li, M. Crocker, Y. Wang, A. Zhu, Catalytic formaldehyde removal by “storage-oxidation” cycling process over supported silver catalysts, Chem. Eng. J. 200–202 (2012) 729–737, <https://doi.org/10.1016/j.cej.2012.06.103>.

[74] E. Kukulska Zajac, K. Góra Marek, J. Datka, IR and TPD studies of the reaction of acetic acid in zeolites NaHY, Microporous Mesoporous Mater. 96 (1) (2006) 216–221, <https://doi.org/10.1016/j.micromeso.2006.06.037>.

[75] A.A. Tsyganenko, F. Can, A. Travert, F. Maugé, FTIR study of unsupported molybdenum sulfide *in situ* synthesis and surface properties characterization, Appl. Catal. A Gen. 268 (1) (2004) 189–197, <https://doi.org/10.1016/j.apcata.2004.03.038>.

[76] T. Liu, X. Li, F. Li, AgNO₃-induced photocatalytic degradation of odorous methyl mercaptan in gaseous phase: mechanism of chemisorption and photocatalytic reaction, Environ. Sci. Technol. 42 (12) (2008) 4540–4545, <https://doi.org/10.1021/es7031345>.